


 Cite this: *CrystEngComm*, 2015, 17, 7930

Anatase/TiO₂-B hybrid microspheres constructed from ultrathin nanosheets: facile synthesis and application for fast lithium ion storage

 Peng Cui,^a Bixia Xie,^a Xiaodan Li,^a Meicheng Li,^{*ab} Yaoyao Li,^a Yu Wang,^a Zhuohai Liu,^a Xin Liu,^a Jing Huang,^a Dandan Song^a and Joseph Michel Mbengue^a

Anatase/TiO₂-B hybrids are considered to be promising anode materials for lithium ion storage. Here, a modified synthesis process for the fabrication of anatase/TiO₂-B hybrid TiO₂ spheres is proposed. Compared to the conventional two-step method employing strong base and acid solutions with titanate as the intermediate, the modified process proposed here employs a one-step reaction which is more facile and moderate. The as-prepared anatase/TiO₂-B hybrid TiO₂ spheres are assembled from ultrathin anatase TiO₂ nanosheets embedded with TiO₂-B nanodomains, which take the advantages of both the anatase and TiO₂-B phases, possessing a large surface area and a hybrid crystalline structure, which are beneficial for fast diffusion and reversible storage of the lithium ions. Therefore, the anodes with the anatase/TiO₂-B hybrid TiO₂ spheres have a capacity of 101 mA h g⁻¹ even at a current density of 20C and good cycling stability. This work provides a facile process for the fabrication of TiO₂ nanostructures with the TiO₂-B phase, which also implies the potential application of anatase/TiO₂-B hybrid spheres in many fields including lithium ion batteries and other electrochemical technologies.

 Received 9th August 2015,
Accepted 12th September 2015

DOI: 10.1039/c5ce01600b

www.rsc.org/crystengcomm

Introduction

Rechargeable lithium ion batteries (LIBs) are attracting enormous interest for practical application in electric vehicles and stationary power storage due to their high energy density, long cycle life and high rate capability.^{1–4} The high capacity and fast charge–discharge capability of the LIBs depend on the advanced materials used in the electrodes.^{5,6} Titanium dioxide (TiO₂) is considered to be a promising anode material for LIBs due to its excellent intrinsic safety, durability, rate capability, moderate theoretical capacity and good chemical stability.^{7–11} However, the typically used TiO₂, *i.e.*, anatase TiO₂, suffers from low lithium ion diffusion capability and poor electronic conductivity which hamper its practical application as an anode material.^{12,13} One polymorph of TiO₂, *i.e.*, TiO₂-B, which has been proposed to be used in LIBs, possesses superior performance over other polymorphs of TiO₂ due to its open channel structure for lithium mobility and characteristic pseudocapacitive behavior, resulting in facile entrance of the Li ions into the crystal structure and faster charge–discharge capability than anatase or rutile.^{7,14–18}

Especially, the hybrid TiO₂, which contains anatase TiO₂ and TiO₂-B, is revealed to perform excellently in LIBs,¹³ deriving from the synergistic effect of the anatase TiO₂ and TiO₂-B with the fast electron transport and lithium diffusion favored by anatase TiO₂ and TiO₂-B, respectively.

The fabrication of a TiO₂ structure composed of pristine TiO₂-B or an anatase/TiO₂-B hybrid generally employs a two-step synthesis process:^{10,19–22} (1) the fabrication of titanate from a strong base (NaOH or KOH) and a Ti-containing precursor solution through hydrothermal synthesis and (2) the exchange of the metal ion with H⁺ to form the H₂TiO₃ precursor by acidification in an acid (typically HCl) solution. After calcination of the H₂TiO₃ precursor at low temperature (typically less than 500 °C), the TiO₂ structure composed of pristine TiO₂-B or the anatase/TiO₂-B hybrid can be obtained. Hence, it is clear that the synthesis process of TiO₂-B is complex. In addition, this synthesis process also limits the growth of TiO₂-B nanostructures on many matrices due to the strong base and acid solutions used for the fabrication of TiO₂-B. Hence, developing a facile synthesis process for TiO₂-B is crucial and necessary for the wide application of TiO₂ materials containing the TiO₂-B phase.

Moreover, the properties and the resultant application of TiO₂-B materials are also governed by their morphologies. Most of the reported TiO₂-B structures, such as nanoparticles,²³ nanotubes,²⁴ nanowires²⁵ and nanorods,²⁶ have some disadvantages including low packing density.

^aState Key Laboratory of Alternate Electrical Power System with Renewable Energy Sources, School of Renewable Energy, North China Electric Power University, Beijing 102206, China. E-mail: mcli@ncepu.edu.cn; Fax: +86 10 6177 2951; Tel: +86 10 6177 2951

^bChongqing Materials Research Institute, Chongqing 400707, China

a poor electronic conduction network due to aggregation. Micrometer-sized materials with a spherical morphology have high packing density and good particle mobility to form a compact electrode layer, which are beneficial to attain high volumetric energy and power density as well as uniform electrode layers.¹⁰ Hence, developing TiO₂ microspheres combining the advantages of the anatase/TiO₂-B hybrid and the spherical morphology will enable the creation of high performance electrodes for LIBs.

Therefore, a facile synthesis process for the anatase/TiO₂-B hybrid microspheres is proposed. The anatase/TiO₂-B hybrid microspheres are constructed from ultrathin nanosheets separated by nanoscale spaces, which show large surface areas (172 m² g⁻¹) and favor the fast diffusion of the ions. By applying them as the anode material in the LIBs, the anatase/TiO₂-B hybrid microspheres were found to exhibit excellent rate performance, demonstrating their ability for fast lithium storage.

Experimental section

Materials synthesis and characterization

TiO₂ spheres were fabricated through hydrothermal synthesis with tetrabutyl titanate (TBOT) and acetic acid as the reactants and AgNO₃ as the agent.²⁷ The concentration ratio of the reactants and AgNO₃ was varied to control the surface morphology of the TiO₂ structures. The reaction time was adjusted from 2 h to 18 h. After the reaction, the precipitate was washed and centrifuged, followed by drying in an oven at 80 °C and calcination at different temperatures. The structure and morphology of the materials were characterized by transmission electron microscopy (TEM, FEI Tecnai F20), scanning electron microscopy (SEM, Hitachi S4800), and X-ray diffraction (XRD, Shimadzu XRD-6000).

Battery fabrication and characterization

The working electrodes were fabricated by coating a slurry containing 70 wt% as-fabricated TiO₂ spheres, 20 wt% acetylene black (Super-P), and 10 wt% polyvinylidene fluoride (PVDF) dissolved in *N*-methyl-2-pyrrolidinone onto a copper foil and dried at 60 °C for 4 h in vacuum (10⁻³ Torr). Then, the sample was dried at 100 °C in vacuum for 12 h before pressing. Standard CR2032-type coin cells were assembled in an Ar-filled glovebox by using the as-prepared anode, a Li metal foil (0.6 mm thick) as the counter electrode, and a separator (Celgard 2400). The electrolyte was 1 M LiPF₆ dissolved in a mixture of ethylene carbonate (EC) and ethyl methyl carbonate (EMC) (v/v = 1:1). The cells were aged for 12 h prior to electrochemical measurements. Galvanostatic discharge-charge (GDC) experiments were performed at different current densities in the voltage window of 0.01–3.00 V with a multichannel battery tester (Land, China). Cyclic voltammetry (CV) measurements were conducted by using an electrochemical workstation (Zahner Zennium). The battery GDC cycling and rate tests were performed with a mass loading of active electrode materials of ~1.05 mg cm⁻².

Results and discussion

The crystalline structure and component features of the as-prepared TiO₂ samples were characterized by the X-ray diffraction patterns shown in Fig. 1a and b. The diffraction peaks of the sample without calcination and the sample calcined at low temperature (250 °C) can be indexed to the combination of H₂TiO₃ and Ti_xO_y. After calcination at 350 °C, which falls in the typically used temperature scale of 300–400 °C for the formation of the TiO₂-B phase in the literature,^{13,18} the sample shows the combined phase of anatase and TiO₂-B phases. The majority of diffraction peaks in the XRD patterns can be indexed to the tetragonal anatase phase (ICDD #00-021-1272), whereas the diffraction peaks from the monoclinic TiO₂-B phase (ICDD #00-046-1237) can also be observed, indicating the coexistence of the anatase phase and the TiO₂-B phase. The TiO₂-B phase tends to transform into anatase when the calcination temperature is increased from 350 °C to 600 °C. As shown in Fig. 1b, the sample calcined at 600 °C shows intense diffraction peaks from the anatase phase and undetectable diffraction peaks from the TiO₂-B phase. In addition, no rutile phase can be observed at such high calcination temperature, probably due to the structural feature of the hybrid spheres and the short calcination time (30 min) for structure reconstruction.²⁸ The phase transformation mainly derives from their different crystallization temperature, which is lower for the TiO₂-B phase. The contents of TiO₂-B calculated from the XRD patterns are 39.9%, 28.2%, 20.3% and 10.2% for the samples calcined at 350 °C, 450 °C, 500 °C and 550 °C, respectively, which are similar to the reported values from the hybrid samples calcined at similar temperatures. It is clear that the presence of the TiO₂-B phase

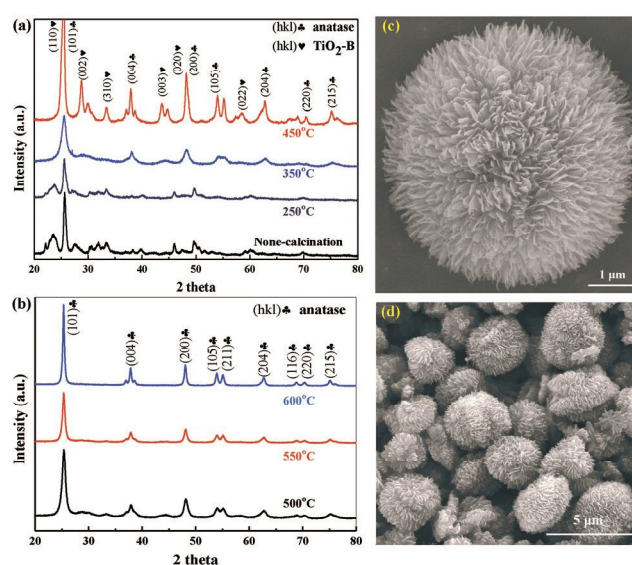


Fig. 1 (a, b) X-ray diffraction (XRD) patterns of the as-prepared TiO₂ samples calcined at different temperatures (no calcination, 250 °C, 350 °C, 450 °C, 500 °C, 550 °C and 600 °C). (c, d) Typical SEM images of an individual TiO₂ sphere (c) and the TiO₂ spheres in bulk calcined at 450 °C.

is governed by the calcination temperature derived from the low phase transformation energy of $\text{TiO}_2\text{-B}$ compared to other TiO_2 polymorphs. Hence, the ratio of the anatase phase to the $\text{TiO}_2\text{-B}$ phase in the anatase/ $\text{TiO}_2\text{-B}$ hybrid materials can be adjusted for various applications by varying the calcination temperature. As the increased content of $\text{TiO}_2\text{-B}$ is accompanied by a faster increase in the content of the anatase phase with increasing calcination temperature from 350 °C to 450 °C, the production of the pure $\text{TiO}_2\text{-B}$ phase is not possible by lowering the calcination temperature. Fig. 1c and d show the typical SEM images of the TiO_2 sample calcined at 450 °C, which displays the spherical structure assembled from the ultra-thin nanosheets.

To further characterize the structural features of the TiO_2 spheres, transmission electron microscopy (TEM) was employed. As shown in the low magnification images in Fig. 2a and b, a TiO_2 sphere is constructed from multiple ultra-thin nanosheets. The nanosheets are composed of multiple fine grains, which make them seem to be porous. In addition, the disperse nanosheets form plenty of nanoscale spaces, which are favorable for ion diffusion and mass transport inside the spheres. The high-resolution TEM (HRTEM) image shown in Fig. 2c shows that the surface of the TiO_2 nanosheets exhibits the $\text{TiO}_2\text{-B}$ phase with lattice spacing values of 0.23 nm and 0.24 nm corresponding to the $(\bar{4}0\bar{1})$ and (202) planes, respectively. The anatase phase can also be observed on the surface of the TiO_2 nanosheets, as depicted in Fig. 2d, which presents typical lattice spacing values of 0.35 nm and 0.24 nm corresponding to the (101) and (004) planes, respectively.

It is clear that the surface of the nanosheet-integrated TiO_2 spheres consists of the anatase and $\text{TiO}_2\text{-B}$ phases. To get an insight into the spatial distribution of $\text{TiO}_2\text{-B}$ and anatase TiO_2 in the spheres, the HRTEM images of the sphere surface containing both the $\text{TiO}_2\text{-B}$ and anatase phases are

shown in Fig. 2e and f. Nanoscale grains can be clearly observed on the surface of the nanosheet-integrated spheres, which possess the typical lattice spacing of $\text{TiO}_2\text{-B}$ planes, indicating the formation of $\text{TiO}_2\text{-B}$ nanodomains on the surface. The grains from anatase TiO_2 can also be observed in the HRTEM images. Considering the major content of the anatase phase in the hybrid revealed by the XRD results, it can be deduced that the as-prepared anatase/ $\text{TiO}_2\text{-B}$ hybrid TiO_2 spheres are assembled from the ultrathin anatase TiO_2 nanosheets embedded with $\text{TiO}_2\text{-B}$ nanodomains. The phase boundaries exist between the anatase phase and the $\text{TiO}_2\text{-B}$ phase, as shown in Fig. 2e, which are expected to be beneficial for the high electrochemical performance of the TiO_2 materials in their application as anode materials for lithium ion batteries. Therefore, the unique structural features of the TiO_2 spheres constructed from the nanosheets and the anatase/ $\text{TiO}_2\text{-B}$ phase boundaries promote their great potential in many fields including lithium ion batteries, catalysts and solar cells.

Furthermore, the morphology of the TiO_2 spheres can be finely controlled by adjusting the precursor concentration. As shown in Fig. 3, by increasing the precursor (TBOT) concentration, the size of the nanosheets is decreased, whereas the density is increased, leading to the much compact TiO_2 spheres. Meanwhile, the size of the TiO_2 spheres is increased from 1–2 μm to 3–5 μm . By adjusting the size and density of the nanosheets, the surface area of the TiO_2 spheres is also modified. For example, in the condition where 0.5 mL of TBOT was added to the reaction solution, the specific surface area (S_{BET}) is around 170 $\text{m}^2 \text{g}^{-1}$, whereas in the condition where 1.0 mL of TBOT was added, the S_{BET} is 86 $\text{m}^2 \text{g}^{-1}$. It is worth noting that the S_{BET} of the as-prepared TiO_2 spheres is much higher than that of the commercial P25 nanoparticles or the anatase TiO_2 spheres, further implying their great potential for application in the electrochemical and catalytic fields.

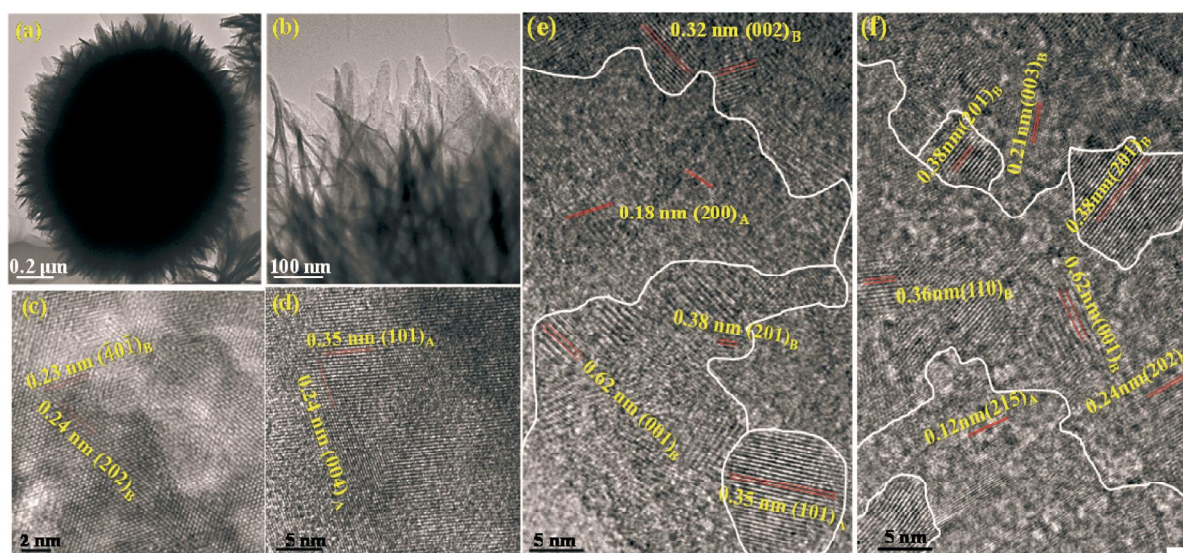


Fig. 2 (a, b) TEM images of a TiO_2 sphere. (c–f) HRTEM images of the surface of the TiO_2 nanosheets constructing the TiO_2 sphere. subscripts represent the anatase phase and the $\text{TiO}_2\text{-B}$ phase, respectively.

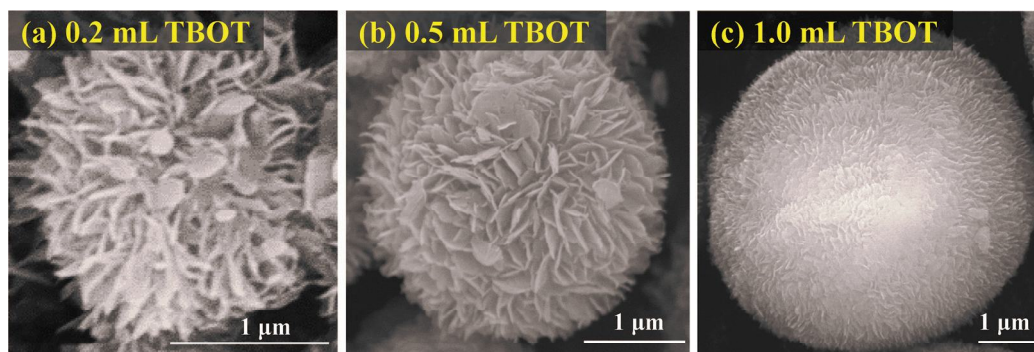


Fig. 3 Typical SEM images of the TiO_2 spheres with different sizes and densities of the nanosheets adjusted by the amount of the TBOT precursor: (a) 0.2 mL, (b) 0.5 mL and (c) 1.0 mL.

From the structural features characterized by the XRD and SEM/TEM measurements, it is shown that the fabrication of the nanosheet-assembled TiO_2 spheres with anatase/ TiO_2 -B hybrid phases is achieved. Compared to the conventional fabrication process of the TiO_2 nanostructures containing the TiO_2 -B phase or the anatase/ TiO_2 -B hybrid phase which employs a hydrothermal reaction in an alkaline (e.g. NaOH) solution followed by acidification to remove the alkali-metal ions, the process used here is much facile and moderate which employs only a one-step hydrothermal reaction in a weakly acidic solution with $\text{C}_2\text{H}_4\text{O}_2$ as the solvent.

To get an insight into the formation mechanism of the TiO_2 spheres with the anatase/ TiO_2 -B hybrid phase from the solution of $\text{C}_2\text{H}_4\text{O}_2$, TBOT and AgNO_3 , the role of AgNO_3 , which is found to be crucial in the reaction process, was investigated. As shown in Fig. 4a, no TiO_2 spheres can be obtained without the addition of AgNO_3 . With the introduction of a small amount of AgNO_3 (0.005 g, Fig. 4b) into the reaction solution, TiO_2 nanowires can be observed in the

product. With a further increase in the amount of AgNO_3 (0.02 g, Fig. 4c), a spot of TiO_2 spheres assembled from nanosheets can be observed in addition to the nanowires. The addition of 0.2 g or more of AgNO_3 to the reaction solution enables the formation of TiO_2 spheres without any nanowires in the product, as can be seen in Fig. 4d. The evolution of the TiO_2 nanostructures with the amount of AgNO_3 indicates the key role of AgNO_3 in the formation of the TiO_2 spheres. The effect of AgNO_3 can be caused by either Ag^+ or NO_3^- . To exclude the effect of NO_3^- , elemental Ag is introduced into the reaction solution, which also enables the fabrication of TiO_2 spheres assembled from nanosheets (Fig. 4e). Hence, the formation of TiO_2 spheres is assisted by the Ag cations. Other types of metal cations, including Zn^{2+} and Cu^{2+} , are also introduced to replace the Ag cations. It is found that only Zn^{2+} promotes the formation of TiO_2 spheres, as presented in Fig. 4f. However, the TiO_2 spheres are compact, which are different from those fabricated with the assistance of Ag cations, indicating the

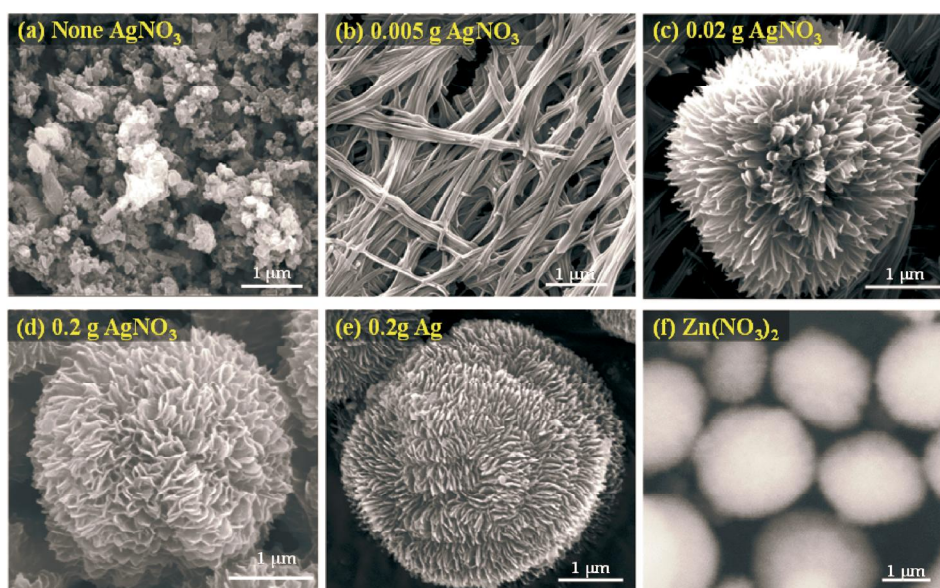


Fig. 4 Typical SEM images of the as-prepared TiO_2 products with different morphologies without or with agents: (a) without the AgNO_3 , (b) with 0.005 g AgNO_3 , (c) with 0.02 g AgNO_3 , (d) with 0.2 g AgNO_3 , (e) with 0.2 g elemental Ag and (f) with $\text{Zn}(\text{NO}_3)_2$.

crucial role of Ag cations in the fabrication of the nanosheet-assembled TiO_2 spheres.

To study the role of Ag in the formation of the TiO_2 spheres, energy-dispersive X-ray (EDX) mapping was carried out to trace Ag signals in the spheres. It is found that the as-fabricated TiO_2 spheres are composed of the elements Ti and O (Fig. 5, inset), without detectable Ag. Considering the lower formation energy of TiO_2 nuclei from hydrolysis of TBOT than that of the Ag atoms or nuclei, Ag is not likely to be present in the core of the TiO_2 nuclei and guide the formation of TiO_2 spheres. Hence, Ag in the form of cations plays an important role in the formation of TiO_2 spheres. It was observed that the presence of Ag^+ in the reaction solution can decrease the hydrolysis rate of TBOT. The hydrolysis of TBOT to form TiO_2 involves the release of Ti cations in the solution. Generally, the release of metal cations can be controlled by the agents releasing anions or cations.²⁹ In the condition where the agent releases anions, the release of metal cations can be enhanced. Hence, the addition of Ag cations can decrease the hydrolysis rate of TBOT by suppressing the release of the Ti cations. In the reaction solution without Ag^+ , the fast hydrolysis of TBOT pushes the TiO_2 concentration to exceed the saturation concentration in a short time, as shown in Fig. 5 (red line), followed by nucleation and crystal growth. Due to the large amount of the nuclei in the reaction solution, the consequent growth on the nuclei will be limited, leading to the formation of the irregular structures (as shown in the inserted SEM images and Fig. 4a). With the assistance of Ag cations, the moderate hydrolysis rate of TBOT enables the gradual nucleation of TiO_2 , followed by the crystal growth on the nuclei to form the nanosheet-assembled TiO_2 spheres.

In addition, the surface morphology of the TiO_2 spheres can also be affected by the addition of Ag cations, probably due to the adsorption of the Ag cations on the surface of the nanostructures which modifies the surface energy of TiO_2 and causes the selective growth along special directions.

Indeed, the TiO_2 spheres fabricated at a high content of Ag cations yield Ag nanoparticles anchored on the nanosheets' surface (revealed by TEM and EDX, data are not shown here in the interest of saving space), which implies the adsorption of Ag on the nanosheets' surface. As can be seen in Fig. 5 (purple line), the initial formation of nuclei and crystal growth also lead to the formation of irregular structures (2 h). With prolonged reaction time, no additional nuclei are formed, and the TiO_2 sites in the solution tend to deposit on the nuclei and grow the nanostructures (6–18 h), *i.e.*, nanosheet-assembled TiO_2 spheres. The diameter of the TiO_2 spheres increases gradually and slowly with the reaction time increasing from 6 h to 18 h, indicating that most of the nanostructures are formed in the time scale of 2–6 h.

Based on these results and discussion, the growth of nanosheet-assembled TiO_2 microspheres may be explained as follows. In the initial stage of the reaction at room temperature, Ag cations are released from AgNO_3 in the reaction solution, which suppress the subsequent release of Ti cations and reduce the generation rate of TiO_2 nuclei. In the following hydrothermal process, the Ag cations are reduced to Ag atoms which adsorb on the surface of the TiO_2 nuclei. The adsorption of Ag hampers the growth of TiO_2 in the corresponding direction, enabling the selective growth of 2D TiO_2 nanosheets. Because the surface of the TiO_2 nuclei is composed of arbitrary planes of TiO_2 , the subsequent growth of the 2D TiO_2 nanosheets is also randomly distributed on the surface of the TiO_2 nuclei. Hence, the nanosheet-assembled microspheres are formed at the end of the reaction.

The electrochemical behavior of the as-prepared TiO_2 spheres was evaluated in lithium half-batteries. Fig. 6a shows the cyclic voltammograms (CV) of the TiO_2 sphere anodes for the first five scans, which were collected at a scan rate of 0.1 mV s^{-1} in a potential window of 1.0–3.0 V vs. Li^+/Li . The TiO_2 sphere anodes present three pairs of redox peaks during the scan process. The dominant A peaks at about 1.73 V/2.0 V correspond to solid-state lithium diffusion in the anatase

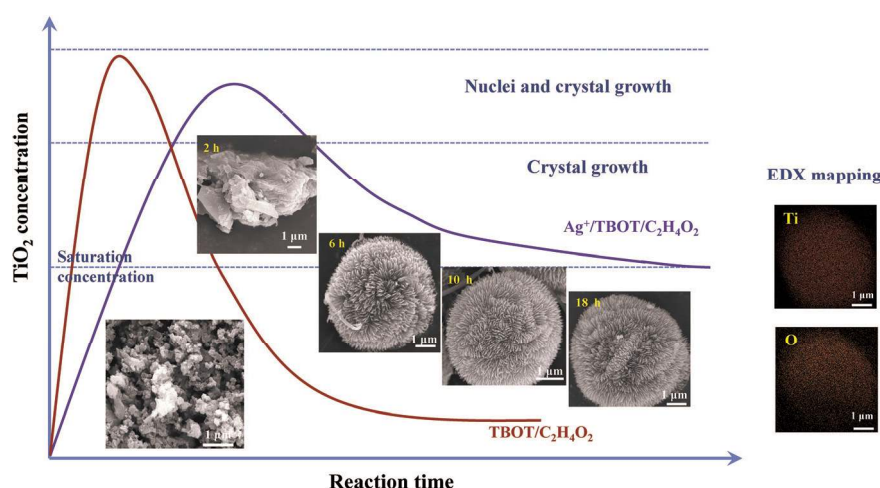


Fig. 5 The formation mechanism of the TiO_2 spheres assembled from the nanosheets.

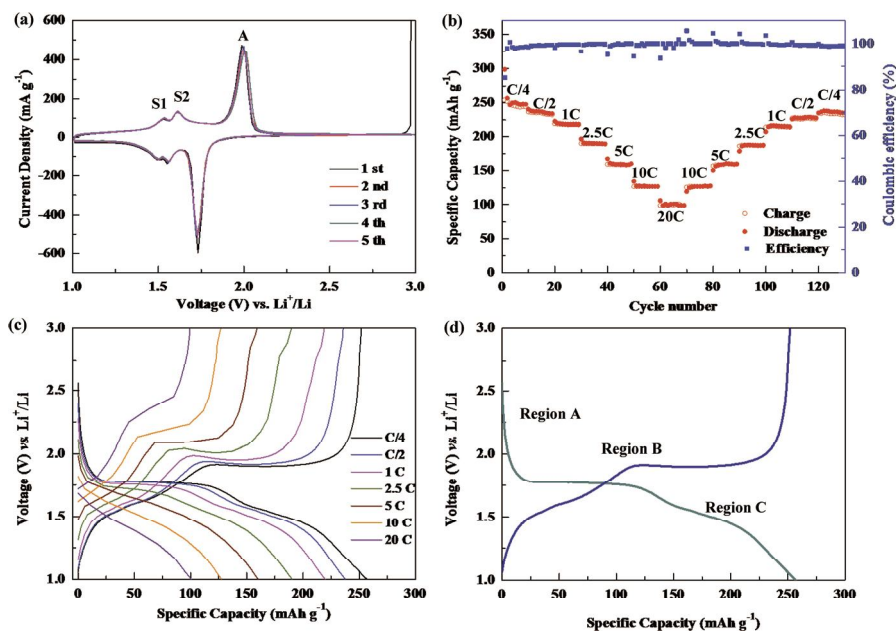


Fig. 6 Electrochemical performance of the anodes with the as-fabricated anatase/TiO₂-B hybrid spheres: (a) Representative CV curves for the 1st, 2nd, 3rd, 4th and 5th cycles at a scan rate of 0.1 mV s⁻¹, (b) rate performance at different current densities, (c) the charge-discharge voltage profiles of the third cycle at different current rates and (d) the charge-discharge voltage profiles at a current rate of C/4 for 5 cycles.

phase, while the two pairs of minor S peaks at 1.56 V/1.61 V and 1.5 V/1.53 V are associated with the pseudocapacitive lithium storage behavior of the TiO₂-B phase.^{13,30} These results demonstrate that the as-prepared TiO₂ spheres integrate the solid-state lithium diffusion process in anatase TiO₂ and pseudocapacitive lithium storage behavior of TiO₂-B. The three pairs of redox peaks are well-defined in the subsequent cycles, indicating the stable Li⁺ insertion/extraction into/out of the TiO₂ sphere anodes. Overall, the as-prepared TiO₂ spheres are expected to yield excellent structural stability during the charge/discharge process.

Fig. 6b shows the cycling performance of the TiO₂ spheres at discharge current densities from C/4 to 20C (1C = 336 mA g⁻¹), then back to C/4 following the same rate steps but in an opposite manner. The discharge capacities at current densities of C/4, C/2, 1C, 2.5C, 5C, 10C, and 20C are about 257, 237, 219, 190, 161, 127, and 101 mA h g⁻¹, respectively. Generally, higher current densities lead to lower specific capacities. With the increase of current density, the specific capacities of the TiO₂ spheres decrease. However, they still exhibit a capacity of about 100 mA h g⁻¹ even at the current density of 20C, indicating the excellent rate performance of the TiO₂ sphere anodes. The outstanding electrochemical performance is attributed to the structural advantages of the TiO₂ spheres in which ultrathin nanosheets with a large surface area could provide high electrode/electrolyte contact area and shorten the diffusion length of lithium ions. More importantly, this material shows 93% of the initial rate capacity (257 mA h g⁻¹) as the current density returns to C/4 (238 mA h g⁻¹), displaying the fine structure stability of the TiO₂ spheres during the charge/discharge process.

Fig. 6c shows the discharge/charge profiles of the TiO₂ sphere anodes at various current densities of C/4, C/2, 1C, 2.5C, 5C, 10C, and 20C in the voltage range of 1.0–3.0 V. At C/4, the TiO₂ spheres exhibit a lithiation capacity of 257 mA h g⁻¹ and a de-lithiation capacity of 252 mA h g⁻¹. Three different voltage regions can be observed in the voltage profiles during the discharge process, as shown in Fig. 6d. Region A displays a rapid potential decrease from the open circuit voltage to about 1.75 V, which corresponds to a solid-solution Li⁺ insertion into the bulk. Then, a plateau is observed in Region B at about 1.75 V, called a two-phase plateau. The plateaus are associated with the phase transition between the tetragonal and the orthorhombic phases due to the lithiation of anatase TiO₂. After the two-phase plateau, Region C from 1.7 to 1.0 V exhibits a sloped domain which can be ascribed to the

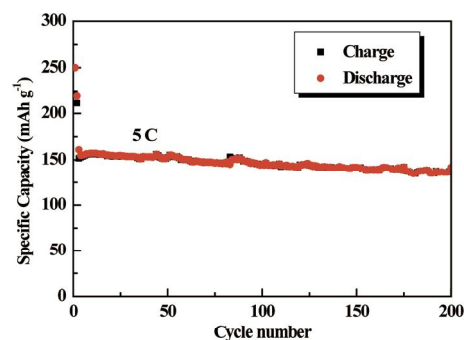


Fig. 7 Cycling performance of TiO₂ sphere anodes at a density of C/4 for the first, C/2 for the second and remaining cycles.

pseudocapacitance and surface reactions of the TiO₂-B phase. Region 3 in the discharge curves also contains the reversible interface lithium storage on anatase and TiO₂-B. The pseudocapacitance of the TiO₂-B phase and favorable charge separation at the phase boundaries of anatase/TiO₂-B collectively contribute to the high capacity and high reversibility of the TiO₂ sphere anodes. Furthermore, the TiO₂ sphere anodes also exhibit enhanced cycling stability, as shown in Fig. 7. The TiO₂ sphere anodes still can retain a capacity of 141 mA h g⁻¹ after 200 cycles at a current density rate of 5C.

The as-fabricated TiO₂ microsphere anodes with anatase/TiO₂-B hybrids exhibit faster lithium storage than various anatase TiO₂ electrodes, including anatase nanoparticles, microspheres, nanowires and nanotubes.^{31–34} Furthermore, the as-prepared TiO₂ sphere anodes present superior reversibility compared to those reported TiO₂-B electrodes,^{35,36} although they may not display greatly high capacity. In the as-prepared TiO₂ microspheres, the dominant anatase TiO₂ is beneficial for maintaining the structural stability, while the surface TiO₂-B phase contributes to fast and vast lithium storage. Therefore, the as-prepared TiO₂ microsphere anodes exhibit high reversibility, fine cycle performance and excellent rate capability.

Conclusion

Anatase/TiO₂-B hybrid spheres constructed from nanosheets were facilely synthesized by a modified hydrothermal process and their formation mechanism was proposed. The modified process employs Ag cations in the reaction solution, which can control the hydrolysis rate of TBOT and enables the formation of spheres constructed from ultrathin nanosheets. The morphology of the TiO₂ spheres and the amount of TiO₂-B in the hybrid can be finely adjusted by varying the precursor solution concentration and calcination temperature. The hybrid TiO₂ spheres possess unique structural features including the hybrid crystalline structure, the large specific surface area and the integration of the nanosheets, which favor the fast diffusion and storage of the lithium ions. Hence, with its application in LIBs, the anode with the as-fabricated TiO₂ spheres maintains a capacity of 101 mA h g⁻¹ at the current density of 20C together with good reversibility after 120 cycles. These results suggest the unique advantage of the synthesis method proposed here and the great potential of the anatase/TiO₂-B hybrid spheres for application in LIBs and other related technologies.

Acknowledgements

This work was supported partially by the National High-Tech R&D Program of China (863 Program, no. 2015AA034601), the National Natural Science Foundation of China (grant no. 91333122, 51402106, 51372082, 51172069, 61204064 and 51202067), the Ph.D. Programs Foundation of the Ministry of Education of China (grant no. 20120036120006 and

20130036110012), the PAR-EU Scholars Program, and the Fundamental Research Funds for the Central Universities.

References

- 1 N.-S. Choi, Z. Chen, S. A. Freunberger, X. Ji, Y.-K. Sun, K. Amine, G. Yushin, L. F. Nazar, J. Cho and P. G. Bruce, *Angew. Chem., Int. Ed.*, 2012, **51**, 9994.
- 2 M. Armand and J. M. Tarascon, *Nature*, 2008, **451**, 652.
- 3 B. Dunn, H. Kamath and J. M. Tarascon, *Science*, 2011, **334**, 928.
- 4 J. B. Goodenough and K. S. Park, *J. Am. Chem. Soc.*, 2013, **135**, 1167.
- 5 X. Li, W. Li, M. Li, P. Cui, D. Chen, T. R. Gengenbach, L. Chu, H. Liu and G. Song, *J. Mater. Chem. A*, 2014, **3**, 2762.
- 6 L. Chu, M. Li, X. Li, Y. Wang, Z. P. Wan, S. Dou, D. Song, Y. Li and B. Jiang, *RSC Adv.*, 2015, **5**, 49765.
- 7 V. Aravindan, Y. S. Lee, R. Yazami and S. Madhavi, *Mater. Today*, 2015, **1**, 345.
- 8 M. Fehse and E. Ventosa, *ChemPlusChem*, 2015, **80**, 785.
- 9 Z. Sun, X. Huang, M. Muhler, W. Schuhmann and E. Ventosa, *Chem. Commun.*, 2014, **50**, 5506.
- 10 H. Liu, Z. Bi, X. G. Sun, R. R. Unocic, M. P. Paranthaman, S. Dai and G. M. Brown, *Adv. Mater.*, 2011, **23**, 3450.
- 11 Z. Genqiang, W. Hao Bin and S. Taeseup, *et al.*, *Angew. Chem., Int. Ed.*, 2014, **53**, 12590.
- 12 N. Takami, Y. Harada, T. Iwasaki, K. Hoshina and Y. Yoshida, *J. Power Sources*, 2015, **273**, 923.
- 13 Q. Wu, J. Xu, X. Yang, F. Lu, S. He, J. Yang, H. J. Fan and M. Wu, *Adv. Energy Mater.*, 2015, **5**, DOI: 10.1002/aenm.201401756.
- 14 Y. Ren, Z. Liu, F. Pourpoint, A. R. Armstrong, C. P. Grey and P. G. Bruce, *Angew. Chem., Int. Ed.*, 2012, **51**, 2164.
- 15 M. Zukalová, M. Kalbá00, L. Kavan, I. Exnar and M. Graetzel, *Chem. Mater.*, 2005, **17**, 1248.
- 16 A. G. Dylla, G. Henkelman and K. J. Stevenson, *Acc. Chem. Res.*, 2013, **46**, 1104.
- 17 H. Liu, Z. Bi, X. G. Sun, R. R. Unocic, M. P. Paranthaman, S. Dai and G. M. Brown, *Adv. Mater.*, 2011, **23**, 3450.
- 18 S. Liu, Z. Wang and Y. Chang, *et al.*, *Adv. Mater.*, 2013, **25**, 3462.
- 19 A. A. Robert, A. Graham, C. Jesús and P. G. Bruce, *Angew. Chem., Int. Ed.*, 2004, **43**, 2286.
- 20 Q. Lei, X. Pan, W. Ling, X. Sun, G. Zhang and X. Guo, *Appl. Catal., B*, 2014, **150**, 544.
- 21 Z. Guo, X. Dong, D. Zhou, Y. Du, Y. Wang, Y. Xia, Z. Guo, X. Dong, D. Zhou and Y. Du, *RSC Adv.*, 2013, **3**, 3352.
- 22 W. A. Daoud and P. GK, *J. Phys. Chem. B*, 2006, **110**, 25746.
- 23 C. Wessel, L. Zhao, S. Urban, R. Ostermann, I. Djerdj, B. M. Smarsly, L. Chen, Y.-S. Hu and S. Sallard, *Chem. – Eur. J.*, 2011, **17**, 775.
- 24 G. Armstrong and A. R. Armstrong, *Chem. Commun.*, 2005, 2454.
- 25 A. R. Armstrong, G. Armstrong, J. Canales, R. García and P. G. Bruce, *Adv. Mater.*, 2005, **17**, 862.
- 26 T. Beuvier, M. Richard-Plouet, M. L. Granvalet, O. Crosnier and L. Brohan, *Inorg. Chem.*, 2010, **49**

- 27 Y. Jiang, M. Li, D. Song, X. Li and Y. Yu, *J. Solid State Chem.*, 2014, **211**, 90.
- 28 H. Dah and C. C. Sorrell, *J. Mater. Sci.*, 2011, **46**, 855.
- 29 G. Gao and Y. Wang, *World Scientific*, 2011, **2**, 581.
- 30 H. Hu, L. Yu, X. Gao, Z. Lin and X. W. Lou, *Energy Environ. Sci.*, 2015, **8**, 1480.
- 31 J. S. Chen and X. W. Lou, *Electrochem. Commun.*, 2009, **11**, 2332.
- 32 K. Jinyoung and C. Jaephil, *J. Electrochem. Soc.*, 2007, **154**, A542.
- 33 H. Ren, R. Yu, J. Wang, Q. Qin, M. Yang, D. Mao, D. Kisailus, H. Zhao and D. Wang, *Nano Lett.*, 2014, **14**, 6679.
- 34 J. Chen, Y. Tan, C. Li, L. Cheah Yan, D. Luan, S. Madhavi, B. Freddy Yin, A. Chiang, A. Lynden and X. Lou, *J. Am. Chem. Soc.*, 2010, **132**, 6124.
- 35 J. Qu, C. Jacqueline, E. Y. Yang, J. Ding and N. Yuan, *ACS Appl. Mater. Interfaces*, 2014, **6**, 22199.
- 36 G. Roberto, M. Michele, M. Luisa De, B. Maria, R. C. Alessandro, S. Teresa, G. Cinzia, C. P. Davide and G. Giuseppe, *ACS Appl. Mater. Interfaces*, 2014, **6**, 1933.